Active segregation in binary mixtures under flow

Giacomo Di Dio[a] and Remy Colin[a]

[a] Max Planck Institute for Terrestrial Microbiology and Center for Synthetic Microbiology (SYNMIKRO), Karl-von-Frisch-strasse 10, 35043 Marburg, Germany

September 20, 2024

Abstract

The spatiotemporal organization of bacteria within complex heterogeneous communities has broad functional impacts that affect many natural and industrial processes. From the gut to the soil, many bacterial environments feature pores and narrow ducts where shear flow is a ubiquitous external physical constraint on motile and sessile bacterial behaviors that might influence the community structure. It is therefore essential to understand how the physics of shear flow contributes to the structuring of complex, phenotypically heterogeneous communities. Here, we investigate experimentally how a model heterogeneous bacterial community of motile and non-motile *Escherichia coli* organizes in a confined environment under Poiseuille flow. We discovered that the mixture actively segregates under flow, with the non-motile population accumulating on one side of the channel, opposite the vorticity direction at the bottom. We demonstrate experimentally and in simulations that this segregation, which depends on motile cell density and flow rate, originates from the rheotactic drift of motile cells that stems from shear acting on their chiral helical flagella. The drifting motile cells collectively induce a conveyer-belt-like backflow advecting the non-motile cells. We also show that non-motile cell accumulation requires sedimentation, which counters flow incompressibility, to take effect. Finally, the segregation of non-motile cells under flow leads at long times to asymmetric mixed biofilm formation in the channel. Our findings reveal a novel mechanism by which physical interactions in flowing environments can drive the spatial organization and long-term dynamics of complex microbial communities.

1 Introduction

Natural microbial communities usually consist of many different species of bacteria, archaea, and eukaryotes, which organize in complex, heterogeneous structures that are important for the functioning of the community, with strong impacts on health, ecology, and industry [1–3]. It is therefore essential to understand the principles governing the organization of these communities. Beyond the many biochemical interactions between microbial species that constrain it [2, 4], the physics of bacterial populations is also increasingly realized to play important roles in their spatial organization, particularly when active bacterial motility drives the population far from equilibrium [5–7].

The most widespread mode of motility is flagellar swimming, whereby bacteria, such as the model organism *Escherichia coli*, propel themselves by rotating their helical flagella and randomly explore the environment by alterning between forward runs and short reorienting tumbles [8]. The micrometric bacteria swimming at $10 - 100\,\mu$m/s elicit low Reynolds number fluid flows, produced by the flagellum and the cell body that can be modeled at first order as an extensile ("pusher") dipole of forces [9]. These flows induce long-range hydrodynamic interactions with other bacteria and the environment, which add to short-range interactions to affect single-cell and population behaviors [10]. Near surfaces, these interactions strongly modify bacterial motion, including surface accumulation [11–14], swimming with a small inward tilt [15–19] and describing circular trajectories [20–23]. In high-density suspensions, interactions between swimmers lead to the emergence of various types of collective motion, dependent notably on the geometrical constraints [24–

27]. In addition to these behaviors observed in phenotypically homogeneous populations, physical interactions have been recently found to also have the potential to shape more complex microbial communities [7, 28–30]. Notably, in mixed motile and non-motile bacterial communities, non-equilibrium density patterns of the non-motile species emerge from swimmer-induced flows [7].

Beyond these cases of suspensions at rest, shear flows in natural environments, such as ocean currents, the soil, pipes, or medical catheters, critically influence the organization of bacterial communities, notably by strongly impacting the physical behavior of both motile and non-motile bacteria [31–34]. Under shear, elongated passive particles rotate following Jeffery‘s Orbits [35] while being advected by the flow. For elongated active particles like bacteria, Jeffery‘s orbiting combines with the ability to cross streamlines to produce non-trivial behaviors. In Poiseuille flow, elongated swimming bacteria describe cycloid trajectories [36, 37] and migrate towards high shear regions [38–42]. The shape of the flagellum, a left-handed helix during propulsion, also leads to sideways rheotaxis. In bulk flow, shear induces a lift force on the chiral flagellum but not on the body. The resulting rheotactic torque orients the swimmer towards the flow vorticity direction, thus generating a rheotactic drift [43–45].

Shear flow combined with surface interactions give rise to even more complex behaviors. Shear flow mitigates cell trapping at surfaces [46]. Surface-aligned swimmers experience an upstream reorientation (weathervane-like effect) that produces upstream motility at low to moderate flow rates, whereas bacteria are advected downstream if the flow is too high [47–49]. For low and intermediate shear rates, bacteria at the surface tend to re-orient towards the vorticity direction via chirality induced rheotaxis [47, 50–53] while at a high enough shear rate, the different surface effects combine to induce an oscillatory surface rheotaxis [50, 53, 54]. Beyond affecting motility, flow has also been long known to influence the structure and dynamics of bacterial colonies and biofilms [55]. This influence can be mechanical [33, 56]. Shear indeed reshapes surface-attached bacterial colonies [57, 58], notably in complex geometries [59–62], and high shear enhances or disrupts biofilms depending on its dynamics [63–66]. Flow also reshapes the landscape of chemical interactions within complex biofilm communities, affecting their composition, dynamics, and evolution [67–72].

Despite the importance of flow for heterogeneous microbial communities, and the latter showing specific physics-driven self-organization behaviors even at rest, the physics of microbes under flow is almost exclusively studied in homogeneous populations of swimming bacteria. Here, we addressed how the physics of active systems affects the organization of heterogeneous communities under flow. We used a binary mixture of motile and non-motile *E. coli*, which we previously established as a tractable model system for heterogeneous bacterial communities [7]. We discovered that the mixture actively segregates in a microfluidic Poiseuille flow. Non-motile cells are advected to the "left" side of the channel (i.e. opposite the vorticity direction) where they accumulate, at a speed that depends on motile cell density and flow rate. We demonstrate experimentally and in simulations that this transport is caused by a backflow that results from the collective chirality-induced rheotactic drift of the surface-oriented motile cells. We also show that non-motile cell accumulation requires sedimentation, which counters the incompressibility of the conveyer-belt-like backflow, to take effect. Finally, we show that this accumulation, which we observe at short time scales, leads at long times to an asymmetric channel colonization via biofilm formation under flow, demonstrating the relevance of this effect to natural microbial community organization.

2 Results

2.1 Leftwards segregation of non-motile bacteria in binary mixtures under flow

To isolate the physical effects of shear flow on the spatial organization of heterogeneous bacterial communities, we employed as a model system a binary mixture of a motile and a non-motile strain of the bacterium *E. coli*. To minimize biological complexity, the strains derive from the same ancestor and differ only in the deletion of the flagellin gene *fliC* in the non-motile one and their tagging with different fluorescent markers (mNeonGreen for the non-motile, mCherry for the motile). We mix the individually pre-grown strains in

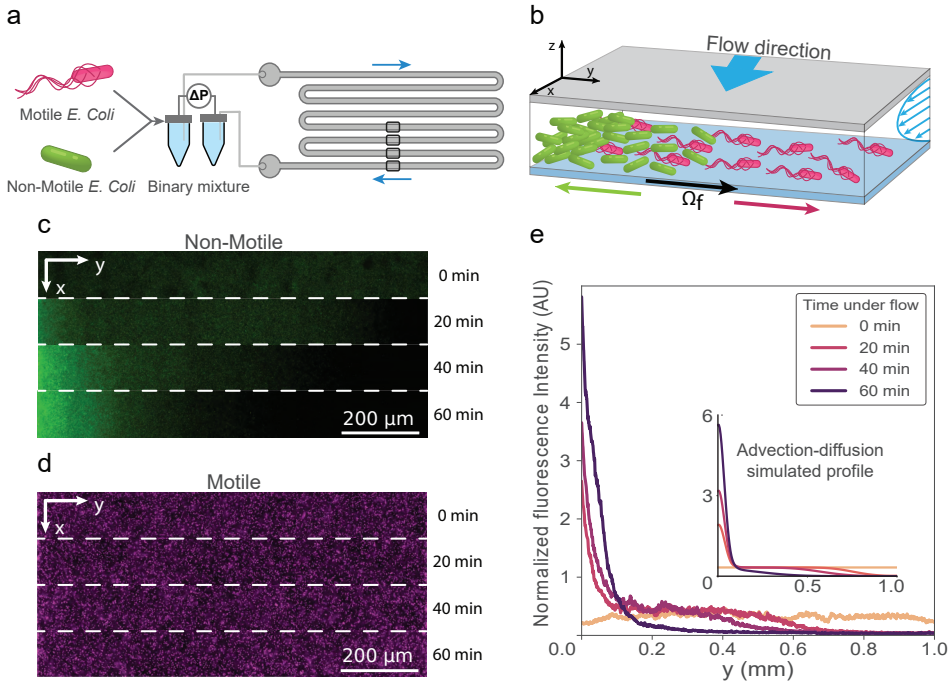

Fig. 1: Active leftward segregation of the non-motile bacteria in binary mixtures under Poiseuille flow. **a** Sketch of the experimental set-up. The spatial organization of the mixture of motile and non-motile *E.coli* is observed under flow at the highlighted positions throughout the channel. **b** Schematic side view of the microfluidic channel. The 'left' side of the channel is defined as facing the flow direction x, i.e. opposite the direction y of the shear vorticity Ω_f at the bottom of the channel. **c,d** Example channel cross-sections of the non-motile (**c**) and motile (**d**) bacterial density, measured via fluorescence at indicated times and 8 μm above the bottom surface **e** Density profiles of non-motile distribution quantified from fluorescence images as in (**c**) of a representative experiment for $\phi_M = 0.17\%$, $\phi_{NM} = 0.17\%$, shear $\dot{\gamma} = 7.5$. The inset shows density profiles from simulations of the one-dimensional advection-diffusion equation (Eq. 2).

controlled proportions in a no-growth motility buffer. The mixture is subjected to Poiseuille flow in a microfluidic channel (height H = 42 μm, width W = 1 mm, total length L = 370 mm), where long straight sections are connected by short serpentine meanders [Fig. 1a].

Following the spatial organization of the mixture via time-lapse fluorescence microscopy over two hours, we observed that the non-motile cells gradually re-distribute and accumulate on the "left" side of the channel when facing the upcoming flow, corresponding to the opposite of the vorticity direction at our observation height (z = 8 μm) [Fig. 1b,c]. In contrast, the distribution of motile bacteria remained homogeneous [Fig. 1d and *SI Appendix*, Fig. S1]. The segregation is absent in control experiments lacking motile cells, indicating that it is driven by their swimming activity. It also results from a local effect: The non-motile density profiles indeed evolve simultaneously and identically across the different straight sections of the chip [*SI Appendix*, Fig. S2a], and the accumulation dynamics are also independent of the number of meanders. The rate of left-side accumulation of non-motile bacteria is independent of their concentration Φ_{NM} [*SI Appendix*, Fig. S2b].

We quantified the evolution of the density profile of non-motile bacteria under flow, which couples the leftward accumulation to a rightward depletion of non-motile cells [Fig. 1e]. This dynamics is well-described by a one-dimensional advection-diffusion equation for low non-motile volume fractions ($\phi_{NM} = 0.17\%$) [Fig.

1e]:

$$\frac{\partial \rho}{\partial t} = \frac{\partial}{\partial y}\left[D\frac{\partial \rho}{\partial y} - v_y \rho\right] \tag{1}$$

with ρ the density of non-motile cells, D their diffusion coefficient, and v_y their drift velocity, taken constant and uniform throughout the bulk of the channel. These cells thus experience a constant uniform advection towards the left that leads to an accumulation at the wall and is eventually balanced by the resulting diffusive counterflux when reaching steady state. At higher concentrations of non-motile bacteria ($\phi_{NM} = 1.7\%$), although still qualitatively correct, this one-dimensional model does not quantify well the accumulation dynamics [*SI Appendix*, Fig. S3], likely because of excluded volume effects.

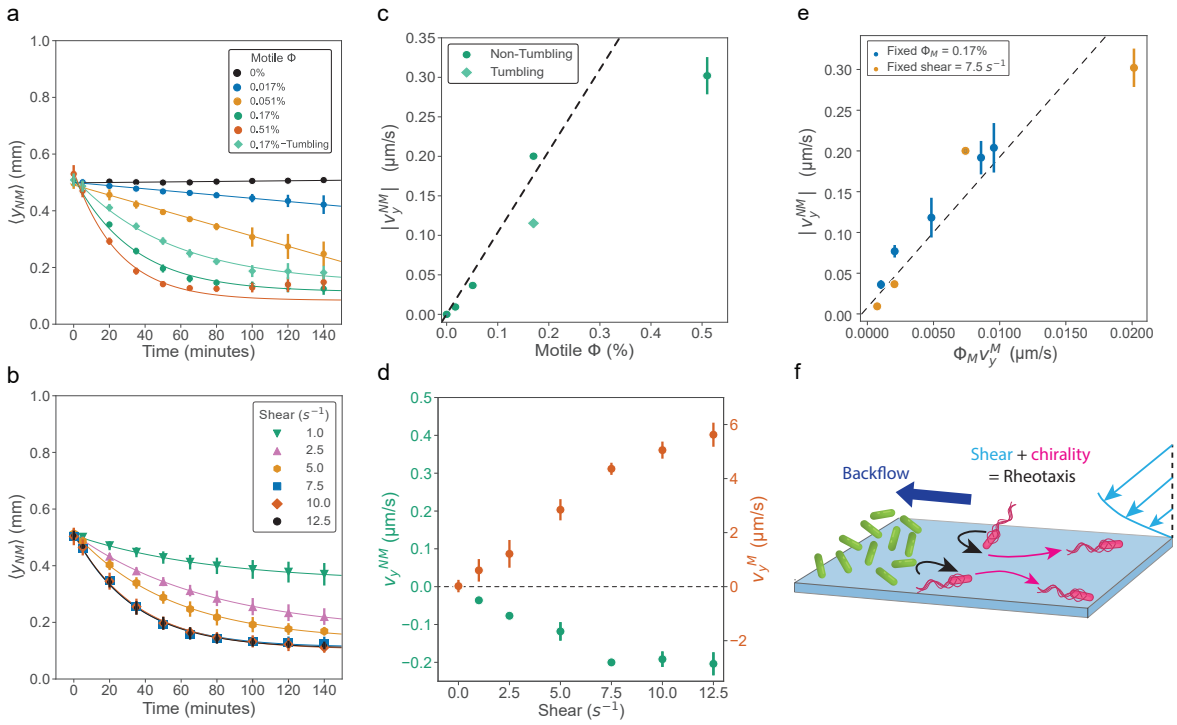

Fig. 2: Non-motile cells leftward advection scales with the rightward rheotactic flux of motile cells. **a,b** Position of the center of mass of non-motile cells as a function of time for (**a**) different motile volume fractions ($\phi_{NM} = 1.7\%$, shear $\dot{\gamma} = 7.5$), and (**b**) increasing values of applied shear ($\phi_M = 0.17\%$, $\phi_{NM} = 1.7\%$). Solid lines are linear (**a** $\phi_M \leq 0.051\,\%$) or saturated exponential fits. **c** Drift velocity of the non-motile center of mass, obtained as the initial slope of the fitting curves of **e**. The dashed line represents a linear fit for non-tumbling data for $\phi_M \leq 0.17\%$ (slope = 0.96 μm/s/%). **d** Drift velocities of non-motile cells v_y^{NM}, extracted from **b**, and the rheotactic velocity of motile cells v_y^M, measured with particle tracking at 2 μm from the bottom surface ($\phi_M = 0.17\%$, $\phi_{NM} = 1.7\%$), as a function of shear. Positive velocities indicate a drift towards the right side of the channel. **e** The relation between the drift of non-motile cells and the rheotactic flux of the motile cells $\phi_M v_y^M$. The dashed line represents a linear fit of all the points with a slope of 20.4. **a-e** Error bars represent the standard deviation (SD) across three biological replicates. **f** Schematics of the putative mechanism driving particle accumulation under shear flow.

2.2 The rheotactic motion of active swimmers drives the drift of passive non-motile cells

To understand the mechanism that underlies this segregation, we then analyzed how the non-motile advection velocity v_y^{NM} depends on possible control parameters. We measured v_y^{NM} from the fluorescence density

profiles via the center of mass (COM) of the distribution of non-motile cells along the width of the channel:

$$\langle y_{NM} \rangle = \frac{\int y\rho(y)dy}{\int \rho(y)dy} = \frac{\sum_i I_i y_i}{\sum_i I_i} \tag{2}$$

with I_i the mNeonGreen fluorescence intensity at pixel i with lateral coordinate y_i, used as a proxy for the local non-motile density $\rho(y)$. The center of mass $\langle y_{NM} \rangle$ starts at mid-channel, reflecting the initially homogeneous non-motile distribution, and drifts leftwards after flow actuation [Fig. 2a,b]. The drift velocity v_y^{NM} of the non-motile bacteria is the initial slope of $\langle y_{NM} \rangle(t)$, which we fitted with saturating exponential or linear functions depending on motile cell density [Fig. 2a]. Both smooth-swimming ($\Delta cheY$) and run-and-tumbling (wild type) *E. coli* drive accumulation, the latter however at a slightly lower rate [Fig. 2a,c]. This indicates that the rate at which swimming direction reorients is a control parameter of the system. Focussing on mixtures with smooth swimmers at a fixed flow rate, we found that the drift velocity first increases linearly with the motile volume fraction, before an inflection above $\phi_M = 0.17\%$ [Fig. 2c]. Hence, the effect of the motile cells is mostly additive, except at higher density where motile cells appear to interact destructively and reduce their individual efficacy.

The accumulation dynamics are also strongly affected by the flow rate experienced by the cells. We observed that the non-motile drift velocity increases linearly as a function of flow rate, quantified by the shear rate at the bottom surface $\dot{\gamma}$, until it reaches a saturation above $\dot{\gamma} = 7.5\ s^{-1}$ [Fig. 2b]. We tracked the motion of the motile cells with particle tracking close to the bottom surface (z = 2 μm) and found that they performed a rheotactic drift in the vorticity direction (the 'right'), as previously reported [43, 54]. The lateral drift velocities of the motile (v_y^M) and the non-motile cells (v_y^{NM}) show a similar dependence as a function of shear rate [Fig. 2d], with v_y^M independent of volume fraction [*SI Appendix*, Fig. S4].

Bringing all our results together, we found that the drift of the non-motile cells v_y^{NM} is a single function of the lateral flux of motile cells $\phi_M v_y^M$, for all motile cells volume fractions and shear rates we probed [Fig. 2e]. This strongly suggests that the non-motile cells are advected by a backflow in reaction to the rheotactic drift of motile cells [Fig. 2f]. In this scenario, the motile cells, which tend to accumulate in equal proportions close to the top and bottom surfaces [*SI Appendix*, Fig. S5] [11, 12], generate low Reynolds number flow fields when swimming, which are additive. The chirality-induced rheotaxis of the swimmers in Poiseille flow then results in a net flux of swimmers. The latter is slightly weaker if the bacteria tumble and therefore randomize their swimming direction more rapidly [45]. This net swimmer flux appears to generate a net backflow in the negative y-direction, which is hence proportional to the strength of the rheotaxis and the number of rheotactic cells. Two elements of this scenario however remain to be elucidated: How is the backflow generated, and how may this incompressible backflow lead to non-motile cell accumulation?

2.3 Sedimentation allows for non-motile bacteria accumulation by countering the conveyor-belt-like recirculation induced by motile cells

We next addressed the question of how the drifting non-motile cells accumulate. We previously showed that sedimentation is necessary for pattern formation in non-flowing binary mixtures [7]. We thus investigated the effect of sedimentation under flow. We prevented sedimentation of the bacteria by matching the volumetric mass of the suspending medium with that of the cells (1.1 g/cm^3), supplementing it with the innocuous density-matching agent iodixanol. We observed that, under the same experimental conditions of previous experiments, the non-motile cell distribution stayed homogeneous in the absence of sedimentation [Fig. 3a].

Nonetheless, the non-motile cells kept being advected. We indeed measured the average drift of both motile and non-motile cells, around the mid-width of the channel, in a vertically resolved manner using φDM image velocimetry [73] and a high motile volume fraction ($\phi_M = 0.51\%$) to make the non-motile drift accurately measurable by this method. For both strains, there are no significant differences between the average drift velocities in sedimenting and non-sedimenting conditions, when they are measurable [Fig. 3b,c]. Indeed, drifts can't be measured above $z \simeq 15\,\mu$m under sedimentation because few if any non-motile cells are visible in the field of view, while the velocities are measurable throughout the channel in the

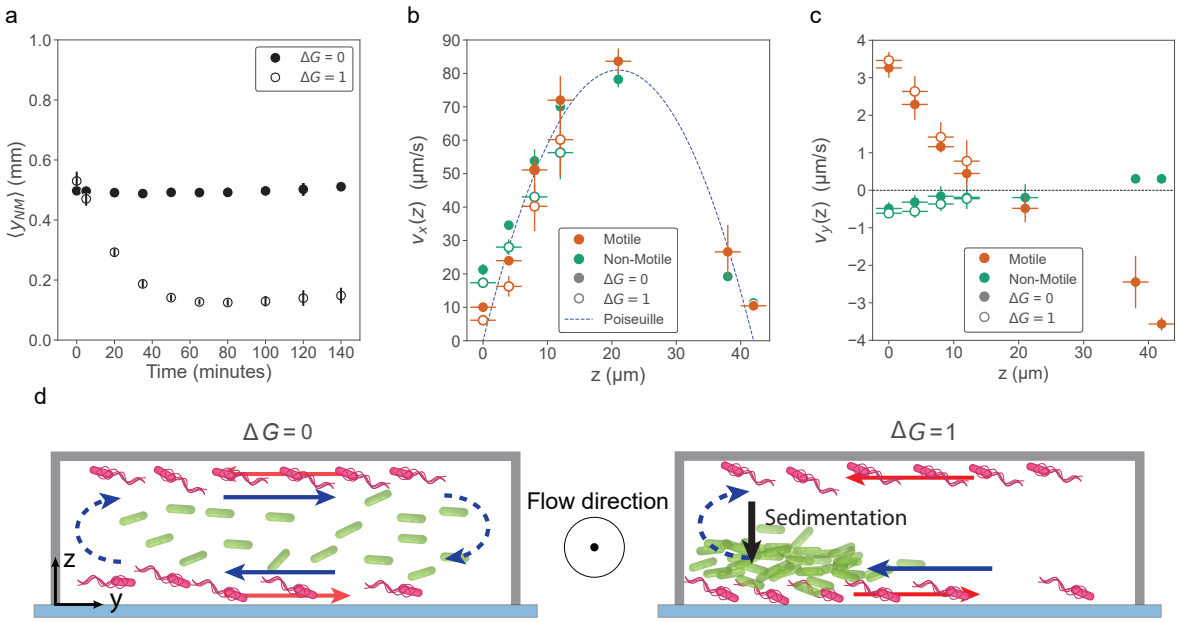

Fig. 3: Sedimentation is necessary for the accumulation of non-motile bacteria that follow a recirculating backflow. **a** Position of the center of mass of non-motile bacteria as a function of time with ($\Delta G = 1$) and without ($\Delta G = 0$, density-matched medium) sedimentation ($\phi_M = 0.51\%$, $\phi_{NM} = 1.7\%$). **b,c** Drift of motile and non-motile cells at increasing distances from the bottom surface, along (**b**) and perpendicular (**c**) to the direction of the main flow, with and without sedimentation, away from the side walls of the channel ($\phi_M = 0.51\%$, $\phi_{NM} = 1.7\%$). Vertical error bars represent the standard deviation across three different measurements, horizontal error bars represent the depth of field ($4\,\mu$m) of the fluorescence microscope. The drift is measured via φDM, except for non-motile cells at z = 38 and 42 μm where particle tracking was used to increase measurement precision (see Methods). **d** Scheme of the accumulation mechanism. Perpendicular to the main flow, motile cells perform chirality-induced rheotaxis (red arrows), resulting in a recirculating, conveyor-belt-like, backflow that advects non-motile cells (blue arrows). Accumulation happens only in the presence of sedimentation (right).

non-sedimenting case. Along the main flow direction ($v_x(z)$), both strains follow the Poiseuille flow profile [Fig. 3b]. Perpendicular to the flow direction, the measurements captured the rheotactic drift of motile bacteria in the vorticity direction and the drift of non-motile cells in the opposite direction [Fig. 3c]. The rheotactic drift $v_y^M(z)$ decreases linearly as a function of height z and changes sign at mid-height, being therefore proportional to the local shear rate as expected from previous results [43]. In particular, the motile rheotactic drift is leftward-oriented at the top of the channel. The non-motile lateral drift $v_y^{NM}(z)$ has an opposite sign to $v_y^M(z)$, and increases as a function of z, also changing sign around mid-channel height, becoming rightward-oriented under the influence of the channel-top leftward-rheotactic motile cells.

From these measurements in the density-matched suspending medium, we deduced that the backflow generated by the rheotactic motile cells takes the form of a recirculating conveyor belt in the y-z plane [Fig.3d]. The fluid incompressibility indeed imposes that the recirculation flows upwards on the left side of the channel, and downwards on the right. Similarly to its role in the absence of flow [7], sedimentation then counteracts the upward flow, effectively compressing the non-motile cells and constraining them to accumulate on the left side.

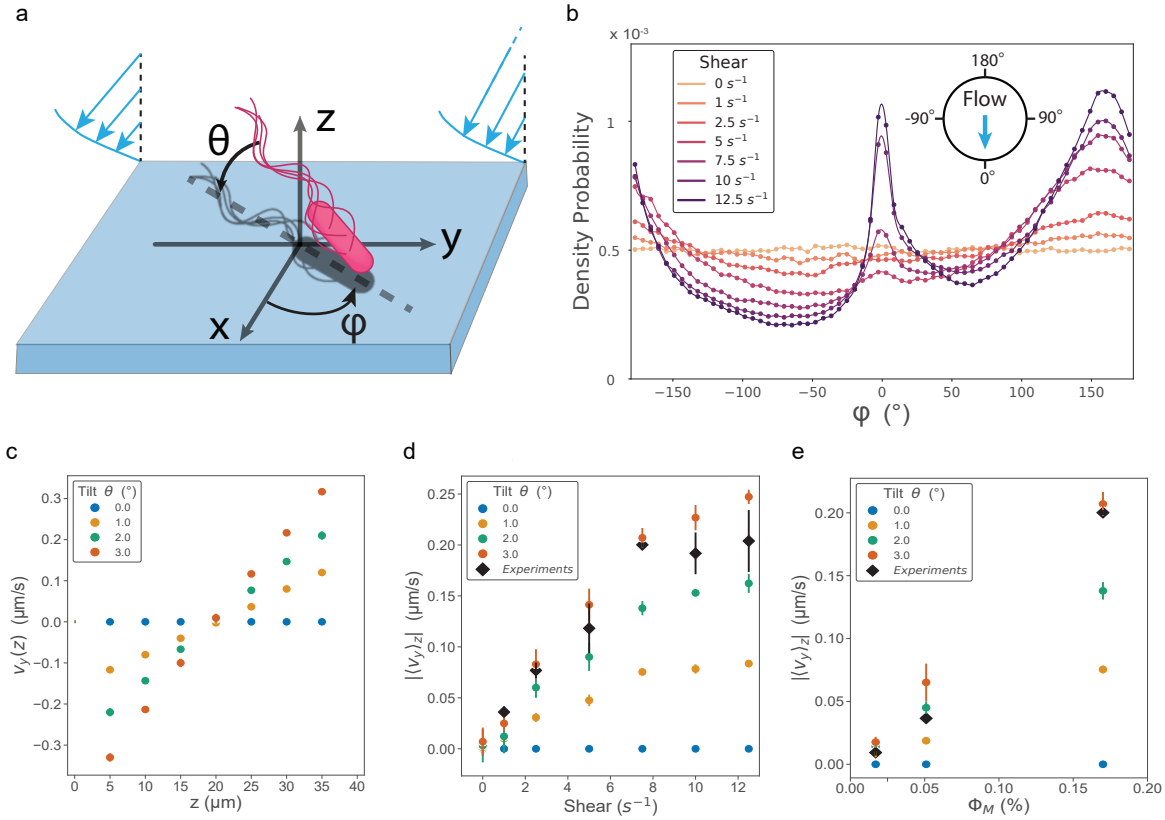

Fig. 4: Rheotactic reorientation of active swimmers generates a backflow comparable to experiments in simulations of tilted force dipoles at surfaces. **a** System of reference for swimmers, with φ the x-y in-plane angle and θ the tilt towards the surface. **b** Distribution of the in-plane angle φ of smooth-swimming *E.coli* under indicated shear, measured with particle tracking in binary mixtures at 2 μm from the bottom surface as the instantaneous velocity direction corrected from Poiseuille flow velocity. **c** Simulated flow velocity in the y direction, generated in the volume of the channel by a distribution of swimmers (ϕ =0.17 %) and averaged across x direction, for varying tilts θ toward the surface. Swimmer orientations follow the distribution measured for a shear of 7.5 s^{-1}. **d,e** Comparison between the simulated average drift of non-motile cells in the y direction, accounting for sedimentation (Eq. 13) and experimental results as a function of shear (**d**) and motile volume fraction (**e**).

2.4 Simulations explain the backflow generation by a distribution of rheotactic swimmers

Since the extensile dipolar flow created by the motile bacteria should be fore-aft symmetric [9], it is at first surprising that the rheotactic bias in the swimming direction can induce a net backflow. Moreover, higher order terms in the flow field predict transport in the opposite direction to the one we observe [74–76]. However, most swimmers are located at the surfaces [*SI Appendix*, Fig. S5], where swimming bacteria are known to be tilted a few degrees ($< 10°$) towards the surface [15–19]. This tilt is also predicted to persist at our shear rates [54]. We hypothesized that it might render the swimmer-induced fluid flow asymmetric, due to a larger effect of friction closer to the wall, which would allow the emergence of the backflow. To test this hypothesis, we simulated the 3D instantaneous flow generated by the bacteria, which we modeled as pusher force dipoles located in equal proportions at the top and bottom surfaces of the channel and tilted with an angle θ [Fig. 4a].

We first measured by particle tracking the experimental distributions of instantaneous bacterial swimming directions in the x-y plane, which are indexed by the angle φ relative to the main flow [Fig. 4a], close to the bottom surface (z = 2 μm) at different shear rates. The distribution of swimming orientation expectedly shows an increasing rightward ($\varphi > 0$) bias as shear increases, similar to previous bulk measurements [45], but also an upstream bias as expected [48] [Fig. 4b].

We then solved the average Stoke's flow generated between two no-slip walls by a population of surface-located tilted dipoles with in-plane orientations drawn from these experimental distributions, using a Fourier-based algorithm [7, 77]. We account for the change of vorticity direction at the top surface by a change of sign of φ for the swimmers there. The simulations indeed produce a swimmers-generated backflow directed toward the left at the bottom and toward the right at the top of the channel [Fig. 4c and *SI Appendix*, Fig. S6]. The flow is an odd linear function of the z-position relative to mid-channel, due to the mirrored distributions of dipole orientations at the top and bottom surfaces. The backflow indeed requires swimmers to be tilted towards the surface ($\theta \neq 0$), which makes the dipolar flow asymmetric and increases with tilt. Realistic flow values are predicted for realistic tilts [Fig. 3c and Fig. 4c].

We next estimated the non-motile drift from the simulated fluid backflow in the presence of sedimentation, and its dependence on swimmer density and shear. The population-averaged non-motile drift is a weighted average of the fluid backflow, $\langle v_y \rangle_z = \int p(z) v_y(z) dz$. The vertical distribution of non-motile cells is given by Boltzmann, $p(z) \propto \exp(-z/L_{sed})$, with the sedimentation length of non-motile bacteria $L_{sed} = 10\,\mu m$, which we measured previously [7]. The simulated drift $\langle v_y \rangle_z$ is non-zero because $p(z)$ is skewed to the bottom, and it accurately reflects the experimental dependence of the non-motile drift both on shear rate [Fig. 4d] and on motile volume fraction – for the low values we simulated [Fig. 4e], with a quantitative match for fairly realistic tilt values $\theta \simeq 3°$ [16–18, 54].

Finally, since realistic flow values are obtained for small tilts, we can write an analytical model for the induced backflow and non-motile drift at first order in tilt (see *Materials and Methods*). As in the simulations, the model predicts a linear backflow as a function of z (Eq. 17), which, when integrated over the Boltzmann distribution, gives the non-motile drift

$$\langle v_y^{NM} \rangle = -\tilde{\kappa} \sin\theta \, h f \left(\frac{h}{L_{sed}} \right) n_M \, v_y^M \tag{3}$$

where $\tilde{\kappa} = 6\pi a^S l_d$ is the normalized dipole strength, with a^S the hydrodynamic radius of the cell body and l_d the dipole length, $n_M = \Phi_M / V_c$ is the motile cell number density and h the half-channel height. The function $f(h/L_{sed})$ increases from 0 to 1 as h/L_{sed} increases from 0 (density match case) to infinity, thus accounting for the effect of sedimentation. The expression also predicts the observed dependence in the bacterial flux $\Phi_M \, v_y^M \propto n_M \, v_y^M$ [Fig. 2c], with a quantitative match given our estimated value of $\tilde{\kappa} = 50\,\mu\text{m}^2$ for a tilt of $\theta \simeq 3°$. Although fairly simple, our model of the underlying physics thus captures well the main features of the system and notably highlights the importance of the tilt of the motile cells at the surface.

2.5 Rheotactic-induced accumulation reshuffles biofilm formation

Finally, we explored the physiological implications of rheotaxis-induced accumulation within microbial communities. For this, we utilized a binary mixture of a wild-type *E. coli* strain and a non-motile *E. coli* strain that are capable of aggregating via *curli* fibers and Antigen 43 expression. Over 48 hours of growth at 30° C in the microfluidic device under the effects of intermediate shear flow (7.5 s^{-1}), we observed that the non-motile fraction of the mixture accumulates at the left side of the chip advected by the rheotactic backflow and forms an asymmetric biofilm at the edge of the channel [Fig. 5a]. This asymmetric biofilm formation is absent in controls with homogeneous populations of non-motile bacteria, which form biofilm on the whole bottom surface of the channel [Fig. 5b]. The composition and development of the biofilm are influenced by the ability of motile bacteria to aggregate through the expression of antigen 43. When motile cells can aggregate, they gradually integrate within the asymmetric biofilm produced by non-motile cells, with most motile cells eventually localizing within the biofilm [*SI Appendix*, Fig. S7a]. In contrast, when

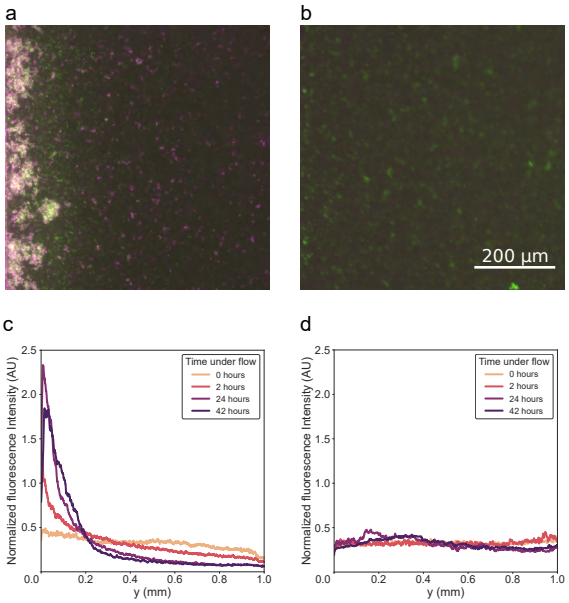

Fig. 5: Rheotaxis-induced accumulation leads to asymmetric biofilm formation in aggregating strains. **a** Biofilm formation on the left side of the channel in a mixture of wild-type motile and non-motile *E. coli* (initial volume fractions: $\phi_M = 0.17\%$, $\phi_{NM} = 0.051\%$). The mixture is imaged after 40 hours under a continuous shear of 7.5 s^{-1}. **b** Homogeneous biofilm formation in a control with only non-motile bacteria. **c,d** Evolution of the density profile of non-motile cells in the channel for the aggregating mixture (**c**) and the control (**d**). In both cases, the profile is calculated as the median over two biological replicates of the fluorescence signal at the 4 positions of the chip highlighted in [Fig. 1].

the motile bacteria cannot express antigen 43, they remain distributed as single cells throughout the channel even after an extended time, as expected in our growth conditions [78, 79]. The biofilm is then almost exclusively composed of non-motile cells and it is generally smaller and less regular in thickness, consistent with the known structural role of flagella in forming robust biofilms in *E. coli* [80], but it remains strongly asymmetric [*SI Appendix*, Fig. S7b]. In both cases, our observations thus show that the interplay between motility and flow can indeed significantly affect over long time scales the patterns of biofilm formation in heterogeneous microbial communities.

Discussion

Fluid flows are a ubiquitous environmental constraint that strongly affects many facets of the behavior of complex microbial communities, particularly in confined and tortuous environments like the animal gut, plant ducts or the soil [32–34]. In particular, the consequences of flow affecting the physics of individual bacterial swimming [47–53, 53, 54] on the structuration of complex, phenotypically and genetically heterogeneous bacterial populations are still being unraveled. Here, we discovered a new type of population structuration under confined flow, where non-motile bacteria in mixed communities with motile ones segregate at the bottom "left" side of microchannels. Combining experiments and modeling, we uncovered the purely physical mechanism driving segregation. The motile cells, which drift rheotactically in the flow vorticity direction ("rightwards" at the bottom), induce a backflow, because they swim with a tilt at the surface that produces asymmetric dipolar flows. Non-motile cell advection by this backflow combines with sedimentation, which breaks vertical symmetry and counters the fluid incompressibility, to allow the passive cells to cross streamlines and accumulate at the left side of the channel. Lastly, this relatively fast segregation mechanism cements at long time in the asymmetric formation of dual biofilms. Hence, this active mechanism drives the

spatial organization of heterogeneous bacterial communities at multiple time scales and over a wide range of physiological densities and relevant shear values, showing its relevance for the many natural microbial communities and biofilms that experience flow.

Although we work at much higher densities, our measurements of motile *E. coli* rheotaxis are in good agreement with previous works that were limited to diluted regimes [43, 45, 47, 50], in particular for the dependence of the lateral motile cell drift on local shear [Figs. 2d, 3c]. Additionally, the distribution of orientations of motile bacteria under shear, which we measured here at the surface, is relatively similar to the one previously measured in bulk [45]. This distribution is also consistent with previous simulations of surface rheotaxis [54], except for the downstream motion probability peak that we observe at higher shear [Fig. 4b], due to downstream swimmers situated further above the surface that Mathijssen *et al* do not consider [54]. For a fixed chiral shape of the flagellum, the strength of rheotaxis depends on the Péclet number $Pe = \dot{\gamma}/D_r$ [45], explaining why tumbling cells, which have a higher effective rotational diffusion coefficient D_r than non-tumbling ones, elicit a weaker non-motile drift [Fig. 2a,c]. Since the rheotactic velocity of motile cells is independent of their volume fraction [*SI Appendix*, Fig. S4], the saturation of $\langle v_y^{NM} \rangle$ at high motile cell density Φ_M [Fig. 2] likely comes from the decrease in the fraction of motile cells that are located at the surface in this case [7].

The presence of backflow in the channel and the advection of non-motile bacteria against the motile cell motion contrasts with previous models and experiments where passive tracers are entrained towards the mean direction of motion of active particles [75, 76]. The segregation mechanism thus provides a different mode of active transport of passive cargoes [81], that notably allows isolating passive from active particles [44, 82]. This difference comes from the dipolar flow field induced by surface swimming bacteria being fore-aft asymmetric, due to the inward tilt that results from short-range interactions with the surface [15–19], whereas a volumetric effect, the Darwin drift, is dominant in the other systems [74–76]. Shear is expected to reduce the tilt at the surface [39], but it can also confer an average tilt to bacteria in the bulk, which would then contribute to the rheotactic backflow [38]. Our simulations and analytical modeling took a simple approach, modeling only the swimmers at the surface as force dipoles, neglecting any steric interactions and Darwin drift, and fixing the tilt angle independently of shear. Despite this simplicity, the model agrees well with experiments for tilt values that are close to the ones expected from simulations [54], indicating that it captures the main physics of the system.

Our findings are relevant to a wide range of microbial communities in many confined environments, from the soil to plants to the animal gut. Indeed, the accumulation mechanism is effective in a wide range of shear values and of physiological volume fractions of motile cells. Moreover, since the rheotactic mechanism is conserved among motile bacterial species [43], the rheotaxis-induced accumulation could reshuffle biofilm formation in many multispecies bacterial communities. All known bacterial flagella are left-handed and rotate counterclockwise during forward-swimming runs [83]. All motile species would thus work in concert, eliciting segregation of the non-motile cells towards the same direction, in highly diverse bacterial communities. Hence, the segregation under shear is expected to be very robust. The asymmetric biofilm formed by the segregated non-motile cells can incorporate motile cells, only if they express antigen 43 as observed in static cultures [78, 79], to form a robust mixed biofilm. In this case, the motile cells thus use pure physics to construct a habitat in the channel that requires the non-motile partner, because motile biofilm formation elsewhere was weak. This effect might benefit the many species that split between motile and non-motile subpopulations upon entry in biofilm-prone stationary phase [6]. Beyond facilitating biofilm formation due to the increased local cell density, the accumulation on the side of the channel, where shear is lower, can also protect the community from flushing by high shear [63, 64]. In summary, the results presented here demonstrate how shear specifically and profoundly affect the spatial organization of heterogeneous bacterial communities over time.

3 Materials and methods

Strains and growth conditions

All strains are derivatives of *Escherichia coli* wild type strain W3110 (RpoS+) and are listed in [*SI Appendix*, Table S1]. All but two strains lack the gene *flu* that encodes for the protein Ag43 mediating cell-cell adhesion at high growth temperatures ($\geq 34°$ C), thus preventing confounding effects of cell aggregation in the segregation dynamics experiments [84]. If not otherwise stated, the motile strain is a $\Delta cheY$ non-tumbling, smooth swimming, mutant. The non-motile strain is a $\Delta fliC$ mutant that lacks flagellar filaments. For fluorescent marking, the strains are transformed with a plasmid with pTRc99a backbone, carrying a fluorescence protein gene under the control of pTac promoter, inducible by Isopropyl-β-d-1-thiogalactopyranoside (IPTG), and an antibiotic (Ampicillin) resistance marker. The non-motile strain is tagged with mNeonGreen and the motile strain with mCherry [7].

Microfluidics and microfabrication

The microfluidic chip used in all the experiments consists of a long, rectangular channel made using soft lithography techniques. The measured channel height is H = 42 μm, the width is W = 1 mm and the channel length is L = 40 mm along the straight sections. The straight parts of the channel are connected through curved meanders for a total channel length of several hundred millimeters. Master molds were fabricated using standard photolithography and microfabrication techniques. The SU82050 photoresist (Microchem^{TM}) was spin-coated on a silicon wafer for 90 s, covered with a positive mask produced using AutoCAD and printed by JD Photo Data (UK), exposed to UV light, baked, and developed according to manufacturer instructions, and silanized. Poly-di-methylsiloxane (PDMS, Sylgard 184, Dow) in a 1:10 crosslinker-to-base ratio was poured on the cast, degassed, baked overnight at 65 °C, peeled off, cut to shape, hole-punched and covalently bound on isopropanol-rinsed microscopy glass slides after oxygen plasma treatment. PDMS to glass covalent bounds were allowed to form for 25 minutes at room temperature and the device was then primed with the binary mixture solution to prevent bubble formation, before connecting it to the pressure pump. For biofilm experiments, the mixture was instead injected 4 hours after the bonding to increase surface hydrophobicity and favor non-motile cells adhesion to the walls of the microfluidic chip. The flow inside the channel is actuated using an external pressure pump (OB1 MK4 microfluidic flow controller, Elvesys) by applying a constant pressure difference in the range of $0.2 - 0.9$ mbar between the inlet and outlet of the chip. We verified the shear rate at the surfaces by measuring the maximum flow rate at the mid-height of the channel using the non-motile cells as tracers.

Binary mixture preparation for segregation dynamics experiments

To prepare the binary mixture used in the experiments, motile and non-motile cells are grown separately overnight in tryptone broth (TB) medium (1% tryptone + 0.5 %wt NaCl) and antibiotic at 37°C. The cells are then diluted 1/100 in 10 mL fresh TB supplemented with 0.1 g/L ampicillin (Amp) and 100 μM IPTG. The strains are then grown separately in a shaking incubator at 270 rpm and 34°C for 4 hours. The bacteria are washed and re-suspended in motility buffer (3.914 g/L NaCl, 10 mM KPO_4 buffer at pH 7, 0.1 mM Ethylenediaminetetraacetate - EDTA) supplemented with 0.01% Tween80 to prevent adhesion to surfaces and 1% glucose to ensure sustained motility throughout the experiment. For the experiments with density-matching media, the cells are instead re-suspended in a solution of motility buffer supplemented with 20% iodixanol ($\rho = 1.11$ g/ml). The optical density (OD) of the resuspended cells is measured and the desired concentrations of motile and non-motile bacteria are obtained by further dilutions. The solutions of motile and non-motile cells are then mixed and the resulting binary mixture is injected into the microfluidic channel.

Binary mixture preparation for biofilm experiments

The bacteria used for the biofilm experiments are *E. coli* wild type (RC 144) or antigen 43 knockout (RC101 - *SI appendix*, Fig. S7), both tagged with mCherry, for the motile strain and *E. coli* Δ*fliC* tagged with mNeonGreen fluorescence protein (SEB 21). The binary mixture is prepared by growing the cells overnight in TB medium and antibiotic at 37° C. Non-motile cells are then diluted 1/50 in M9 medium (Na_2HPO_4 48 mM + KH_2PO_4 22 mM + NaCl 8.4 mM + NH_4 Cl 18.6 mM + $MgSO_4$ 2 mM + $CaCl_2$ 1 mM) supplemented with 0.4% succinate and 0.2% casaminioacids, 0.1 g/L Ampicillin and 100 μM IPTG. The motile strain is prepared in TB as described in the previous section. Cells are grown at 30°C, where they form robust biofilms [85], in a shaking incubator at 270 rpm. The motile strain is grown for 5 hours, and the non-motile strain for 8 hours to ensure that bacteria are in the late exponential/early stationary phase where *curli* expression is high. The bacteria are then washed and re-suspended in the filtered spent M9 medium in which the non-motile strain was grown, since it promotes biofilm formation, in contrast to fresh medium that induces biofilm-repressing exponential growth. The mixture is injected into the microfluidic chip and left to rest for one hour to promote adhesion, before flowing filtered spent M9 medium into the channel. The evolution of the mixture is observed at several positions through the channel for a total duration of 42 hours under a constant shear of 7.5 s^{-1} and a temperature of 30°C.

Images and video acquisition

The images and videos are acquired using a Nikon TI-E inverted fluorescence wide-field microscope with a 20X (NA 0.75) objective, mCherry (excitation filter 572/25, emission 645/90) and GFP (excitation filter 470/40, emission 525/50) filter cubes, and an Andor Zyla sCMOS Camera (1 px = 0.35 μm), piloted via the Nikon NIS software. The depth of field of the objective is around 4 μm. Focus is maintained using the Nikon perfect focus system. For the measurements of bacterial drift, videos of 5 seconds at 100 fps are captured at different distances from the bottom surface away from the lateral walls. For the analysis of swimming trajectories with particle tracking, videos are captured at 50 fps for 40 seconds with a 2x2 pixel binning at 2 μm from the bottom surface.

Segregation dynamics experiments

For measuring the density profiles, images are captured at 6 different points (respectively at 25, 130, 210, 255, 300, and 345 mm from the inlet) in the middle of the straight portion of the channel, at 8 μ m from the bottom surface. Images are recorded before (0 min) and 5, 20, 35, 50, 65, 80, 100, 120, and 140 minutes after the actuation of the flow. Since the image size for 20X magnification is 665×665 μm^2, two images are captured and stitched together to visualize the whole channel width (1 mm) at each point. The fluorescence intensity profiles of each image are extracted with ImageJ after subtracting black noise and correcting for the inhomogeneous illumination profile. At each position, fluorescence intensity profiles are then stitched, normalized to the total fluorescence intensity of the image, and plotted with custom Python scripts.

The center of mass is extracted from the fluorescence intensity profiles via Eq. 2 at each position and averaged over the 4 positions that are furthest from the inlet, to limit the effect of cells being washed out close to the inlet. The center of mass is then plotted as a function of time for different volume fractions, and fitted with a linear function $\langle Y_{NM} \rangle(t) = a \cdot t + b$ for $\phi_M < 0.17\%$ or a saturating exponential $\langle Y_{NM} \rangle(t) = a\tau(1 - e^{-\frac{t}{\tau}}) + (S - a\tau)$ otherwise. The drift of the particles is then estimated from the initial slope (a) extracted from these curves.

Measurements of bacteria drift

To measure the drift of both motile and non-motile particles, videos are acquired in the relevant fluorescence microscopy channel at different distances from the bottom surface far from the lateral walls (minimum distance: 100μm). To prevent the accumulation of non-motile cells on the sides, the videos are captured 30 seconds after the actuation of the flow, and then the flow is reversed for 30 seconds. The videos are then

analyzed with the φDM image velocimetry algorithm to extract the population-averaged drift in the field of view [73]. For measurements with density-matching media near the top of the microfluidic channel, we used particle tracking instead of φDM image velocimetry to minimize the influence of particles below the focal plane, which can appear as background drift in the field of view and reduce the precision of velocimetry measurements.

Swimming trajectories analysis with Particle tracking

To analyze the rheotactic trajectories of *E.coli* in our system, we employed a binary mixture of *E. coli*, consisting of a non-fluorescently labeled non-motile strain at 1.7% volume fraction and a non-tumbling motile strain at different volume fractions (0.51%, 0.17%, 0.051%, and 0.017%). Since particle tracking works best at low cell density, we used a mix where only a fraction of the motile cells are fluorescently labeled (labeled volume fraction: $3.4 \cdot 10^{-3}$ %). Using fluorescence microscopy, we captured videos of swimming cells away from the lateral walls, $2\mu m$ from the bottom surface at different values of imposed shear. Using a custom-made particle tracking ImageJ plugin [86], we analyzed the trajectories of the swimming bacteria and extracted the instantaneous orientation of the cells as $\varphi = \arctan(\frac{\Delta y}{\Delta x})$, with Δx and Δy the change in the x and y position of the swimmers between frames, corrected for the flow speed inferred from the Poiseuille flow profile.

Unidimensional drift-diffusion simulations

In Fig. 1d, we employed a finite difference method to solve the advection-diffusion equation describing the system Eq. (1). We discretized the advection-diffusion equation with the Euler integration method as

$$\rho(y, t + \Delta t) = \rho(y, t) + F(\rho(y + \Delta y, t) - 2\rho(y, t) + \rho(y - \Delta y, t)) - G(y)\left(\rho(y, t) - \rho(y - \Delta y, t)\right) \quad (4)$$

where

$$F = \frac{D \cdot \Delta t}{(\Delta y)^2} \quad (5)$$

$$G(y) = \frac{V(y) \cdot \Delta t}{\Delta y} \quad (6)$$

We set the initial density as $\rho(y, t = 0) = 1$, i.e. homogeneous across the spatial domain. We simulated the system for a total time of T = 7200 s, with a diffusion constant of D = 5 $\mu m^2/s$ and a total length of L = 1000 μm. $\Delta y = 5$ μm represents the spatial grid spacing and $\Delta t = 1$s represents the temporal grid spacing for simulating the evolution of the density profile. We defined the velocity V(y) to rise linearly from 0 to 0.20 $\mu m/s$ over the first 50 μm, remain constant in the middle section, and decrease linearly back to 0 over the last 50 μm. We used a non-constant velocity to simulate the effect of lateral surfaces on the swimmer-induced flow, though we obtained similar qualitative results with constant velocity.

Numerical Simulations

We performed the simulations in a three-dimensional rectangular box of width and length W = 256 μm and height H = 40 μm. The applied boundary conditions are periodic boundary conditions at the lateral walls of the box and no-slip boundary conditions at the top and bottom walls. We run the simulations with a variable number of swimmers that for the dimensions of the rectangular box correspond to a volume fraction of 0.017 %, 0.051 %, and 0.17 %. The swimmers are modeled as a pusher dipole of point forces, one representing the body and the other the flagellum. The magnitude of both point forces is $f_0/6\pi\eta = a^S v_0$, with η the fluid viscosity, $a^S = 0.7\mu$m the hydrodynamic radius of the cell body, and $v_0 = 30\mu m/s$ the swimming speed. In this context, The fluid flow $\mathbf{v^{i \leftarrow j}}$ at position $\mathbf{r}_i$ generated by a point force $\mathbf{f}_j$ positioned at $\mathbf{r}_j$ is given by :

$$\mathbf{v}^{i \leftarrow j} = \mathbf{\Omega}^{i \neq j}(\mathbf{r_i}, \mathbf{r_j}) \cdot \frac{\mathbf{f_j}}{\mathbf{6}\pi\eta} \quad (7)$$

where $\mathbf{\Omega}^{i\neq j}$ is the normalized hydrodynamic-interaction tensor (the normalized Green function) of the incompressible Stokes equation:

$$-\nabla p + \eta \nabla^2 \mathbf{v} + \mathbf{f} = 0 \tag{8}$$

$$\nabla \cdot \mathbf{v} = 0 \tag{9}$$

We take advantage of the 2D decomposition in Fourier space of the flow field between two parallel plates and its corresponding Oseen tensor $\mathbf{\Omega}^{i\neq j} = \sum_{\mathbf{k}} \omega^{i\neq j}(\mathbf{k}, \mathbf{z_i}, \mathbf{z_j})$ developed in [77, 87]. In this method, a no-net-flow condition is imposed on the edges of the simulation box, which yields a non-zero $\mathbf{k} = 0$ term in the Fourier decomposition that compensates for the backflow induced by the point force. We therefore can use this term to compute the mean backflow $\mathbf{v}(\mathbf{z_i})$ induced by a population of N swimmers as [7, 77]:

$$v_\alpha(z_i) = -\frac{3\pi}{W^2 h} \sum_{j=1}^{2N} \bar{\omega}(z_i, z_j) a^S v_\alpha^j(z_j) \tag{10}$$

with

$$\bar{\omega}(z_i, z_j) = \frac{3}{4} \frac{(h^2 - z_j^2)(h^2 - z_i^2)}{h^2} + \left(z_j z_i + |z_j - z_i| h - h^2\right) \tag{11}$$

where $h = H/2$ is half the channel height, with the vertical positions z_i, $z_j \in [-h, h]$. The indices $\alpha = x, y$ correspond to the horizontal space directions only ($v_z = 0$), and $a^S v_\alpha^j(z_j)$ are the horizontal components of the $2N$ normalized point forces since each swimmer is modeled as a force dipole. The latter are assigned to the top and bottom surfaces in equal numbers and have an orientation

$$\mathbf{u_j} = \begin{pmatrix} \cos\varphi_j \cos\theta \\ s_j \sin\varphi_j \cos\theta \\ -s_j \sin\theta \end{pmatrix} \tag{12}$$

The polar angle φ_j was drawn from the distributions of Fig. 4b. The tilt angle θ, which represents the inclination of the swimmer towards the surface, was fixed for a given simulation. The parameter s_j accounts for the mirroring at the top of the channel of the tilt and of the distribution of φ, due to the change in vorticity direction, with s_j = 1 at the bottom and s_j = -1 at the top. For each swimmer, the cell body is located in $z_{B,j} = s_j(z_m - h)$ and produces the reduced force $+a^S v_0 \mathbf{u_j}$ and the flagellum is in $z_{F,j} = s_j(z_m - h) + s_j l_d \sin\theta$, with the reduced force $-a^S v_0 \mathbf{u_j}$, where $l_d = 4\mu$m the fixed dipole length and $z_m = 0.5\mu$m is the fixed distance between the cell body and channel wall. Varying the distance z_m had only fairly small quantitative effects on the simulated flow field [*SI Appendix*, Fig. S6]. We use our previous implementation of [77] to compute $\langle u_\alpha^i(z_i)\rangle$ [7].

Finally, we compute the population averaged drift of non-motile cells in Fig. 4d,e as

$$\langle v_y \rangle_z = \int_{z=\epsilon}^{z=H-\epsilon} p(z) v_y(z) dz \tag{13}$$

where $z = z_i + h$, $\epsilon = 2\,\mu$m is a bacteria-sized cutoff to avoid the unphysical behavior next to point forces, and $p(z)$ is the vertical distribution of non-motile cells, which is skewed by sedimentation and is given by the Boltzmann distribution:

$$p(z) = \frac{1}{L_{sed}} \frac{\exp(-z/L_{sed})}{1 - \exp(-H/L_{sed})} \tag{14}$$

where $L_{sed} = 10\,\mu$m is the sedimentation length of non-motile particles [7].

Analytical model

We can deduce from Eq. 10 an expression for the flow created by the N dipoles with cell bodies in z_j and flagella in $z_j + \delta z_j$, with the tilt $\delta z_j = l_d \sin\theta_j$:

$$v_\alpha^i(z_i) = -\frac{3\pi h a^S}{W^2} \sum_{j=1}^{N} \omega^D(\tilde{z}_i, \tilde{z}_j, \delta\tilde{z}_j) v_\alpha(\tilde{z}_j) \tag{15}$$

where $v_\alpha(\tilde{z}_j)$ is the speed of swimmer j, $\tilde{z} = z/h$ and at first order in $\delta\tilde{z}_j$:

$$\omega^D(\tilde{z}_i, \tilde{z}_j, \delta\tilde{z}_j) = \left[\frac{3}{2}\left(1 - \tilde{z}_i^2\right)\tilde{z}_j - \tilde{z}_i + \mathrm{sign}\left(\tilde{z}_i - \tilde{z}_j\right)\right]\delta\tilde{z}_j \tag{16}$$

In the simple case of surface localized swimmers with a fixed tilt that perform rheotaxis under Poiseuille flow, since the tilt and the rheotactic drift both change sign from the top to the bottom wall, the backflow they generate in the y-direction is easily deduced as:

$$v_y^{NM}(z_i) = 6\pi a^S l_d \, n_M \, v_y^M \sin\theta \, z_i \tag{17}$$

where we introduced the swimmer number density $n_M = N/W^2 H = \Phi_M/V_c$ and v_y^M is the chemotactic drift of the cells at the bottom of the chamber. If we integrate on the Boltzmann distribution of non-motile bacteria (Eq. 14), we obtain the mean advection speed

$$\langle v_y^{NM} \rangle = -3\pi a^S l_d \sin\theta \, H f\left(\frac{H}{2L_{sed}}\right) n_M \, v_y^M \tag{18}$$

with

$$f(x) = \frac{1}{\tanh(x)} - \frac{1}{x} \tag{19}$$

increasing from 0 to 1 as $H/2L_{sed}$ increases from 0 (density matched case) to infinity.

References

[1] Cordero, O. X. & Datta, M. S. Microbial interactions and community assembly at microscales. *Current Opinion in Microbiology* **31**, 227–234 (2016).

[2] Nadell, C. D., Drescher, K. & Foster, K. R. Spatial structure, cooperation and competition in biofilms. *Nature Reviews. Microbiology* **14**, 589–600 (2016).

[3] Sauer, K. *et al.* The biofilm life cycle: expanding the conceptual model of biofilm formation. *Nat Rev Microbiol* **20**, 608–620 (2022).

[4] Eigentler, L., Davidson, F. A. & Stanley-Wall, N. R. Mechanisms driving spatial distribution of residents in colony biofilms: An interdisciplinary perspective. *Open Biology* **12**, 220194 (2022).

[5] Cates, M. E. Diffusive transport without detailed balance in motile bacteria: Does microbiology need statistical physics? *Rep. Prog. Phys.* **75**, 042601 (2012).

[6] Colin, R., Ni, B., Laganenka, L. & Sourjik, V. Multiple functions of flagellar motility and chemotaxis in bacterial physiology. *FEMS Microbiology Reviews* **45**, fuab038 (2021).

[7] Espada Burriel, S. & Colin, R. Active Density Pattern Formation in Bacterial Binary Mixtures. *PRX Life* **2**, 023002 (2024).

[8] Berg, H. C. & Anderson, R. A. Bacteria Swim by Rotating their Flagellar Filaments. *Nature* **245**, 380–382 (1973).

[9] Drescher, K., Dunkel, J., Cisneros, L. H., Ganguly, S. & Goldstein, R. E. Fluid dynamics and noise in bacterial cell–cell and cell–surface scattering. *Proceedings of the National Academy of Sciences of the U. S. A.* **108**, 10940–10945 (2011).

[10] Elgeti, J., Winkler, R. G. & Gompper, G. Physics of microswimmers—single particle motion and collective behavior: A review. *Rep. Prog. Phys.* **78**, 056601 (2015).

[11] Li, G. & Tang, J. X. Accumulation of Microswimmers near a Surface Mediated by Collision and Rotational Brownian Motion. *Physical Review Letters* **103**, 078101 (2009).

[12] Berke, A. P., Turner, L., Berg, H. C. & Lauga, E. Hydrodynamic Attraction of Swimming Microorganisms by Surfaces. *Physical Review Letters* **101**, 038102 (2008).

[13] Li, G. *et al.* Accumulation of swimming bacteria near a solid surface. *Physical Review E* **84**, 041932 (2011).

[14] Giacché, D., Ishikawa, T. & Yamaguchi, T. Hydrodynamic entrapment of bacteria swimming near a solid surface. *Physical Review E* **82**, 056309 (2010).

[15] Spagnolie, S. E. & Lauga, E. Hydrodynamics of self-propulsion near a boundary: Predictions and accuracy of far-field approximations. *Journal of Fluid Mechanics* **700**, 105–147 (2012).

[16] Sipos, O., Nagy, K., Di Leonardo, R. & Galajda, P. Hydrodynamic Trapping of Swimming Bacteria by Convex Walls. *Physical Review Letters* **114**, 258104 (2015).

[17] Bianchi, S., Saglimbeni, F. & Di Leonardo, R. Holographic Imaging Reveals the Mechanism of Wall Entrapment in Swimming Bacteria. *Physical Review X* **7**, 011010 (2017).

[18] Bianchi, S., Saglimbeni, F., Frangipane, G., Dell'Arciprete, D. & Leonardo, R. D. 3D dynamics of bacteria wall entrapment at a water–air interface. *Soft Matter* **15**, 3397–3406 (2019).

[19] Mousavi, S. M., Gompper, G. & Winkler, R. G. Wall entrapment of peritrichous bacteria: A mesoscale hydrodynamics simulation study. *Soft Matter* **16**, 4866–4875 (2020).

[20] Lauga, E., DiLuzio, W. R., Whitesides, G. M. & Stone, H. A. Swimming in circles: Motion of bacteria near solid boundaries. *Biophysical Journal* **90**, 400–412 (2006).

[21] DiLuzio, W. R. *et al.* Escherichia coli swim on the right-hand side. *Nature* **435**, 1271–1274 (2005).

[22] Li, G., Tam, L.-K. & Tang, J. X. Amplified effect of Brownian motion in bacterial near-surface swimming. *Proceedings of the National Academy of Sciences of the U. S. A.* **105**, 18355–18359 (2008).

[23] Di Leonardo, R., Dell'Arciprete, D., Angelani, L. & Iebba, V. Swimming with an Image. *Physical Review Letters* **106**, 038101 (2011).

[24] Dombrowski, C., Cisneros, L., Chatkaew, S., Goldstein, R. E. & Kessler, J. O. Self-Concentration and Large-Scale Coherence in Bacterial Dynamics. *Physical Review Letters* **93**, 098103 (2004).

[25] Sokolov, A., Aranson, I. S., Kessler, J. O. & Goldstein, R. E. Concentration Dependence of the Collective Dynamics of Swimming Bacteria. *Physical Review Letters* **98**, 158102 (2007).

[26] Wioland, H., Lushi, E. & Goldstein, R. E. Directed collective motion of bacteria under channel confinement. *New Journal of Physics* **18**, 075002 (2016).

[27] Colin, R., Drescher, K. & Sourjik, V. Chemotactic behaviour of Escherichia coli at high cell density. *Nature Communications* **10**, 5329 (2019).

[28] Williams, S., Jeanneret, R., Tuval, I. & Polin, M. Confinement-induced accumulation and de-mixing of microscopic active-passive mixtures. *Nat. Commun.* **13**, 4776 (2022).

[29] Bouvard, J., Moisy, F. & Auradou, H. Ostwald-like ripening in the two-dimensional clustering of passive particles induced by swimming bacteria. *Physical Review E* **107**, 044607 (2023).

[30] Grober, D. *et al.* Unconventional colloidal aggregation in chiral bacterial baths. *Nature Physics* **19**, 1680–1688 (2023).

[31] Barnett, B. J. & Stephens, D. S. Urinary Tract Infection: An Overview. *The American Journal of the Medical Sciences* **314**, 245–249 (1997).

[32] Wheeler, J. D., Secchi, E., Rusconi, R. & Stocker, R. Not Just Going with the Flow: The Effects of Fluid Flow on Bacteria and Plankton. *Annual Review of Cell and Developmental Biology* **35**, 213–237 (2019).

[33] Krsmanovic, M. *et al.* Hydrodynamics and surface properties influence biofilm proliferation. *Advances in Colloid and Interface Science* **288**, 102336 (2021).

[34] Padron, G. C., Shuppara, A. M., Palalay, J.-J. S., Sharma, A. & Sanfilippo, J. E. Bacteria in Fluid Flow. *Journal of Bacteriology* **205**, e0040022 (2023).

[35] Jeffery, G. B. The Motion of Ellipsoidal Particles Immersed in a Viscous Fluid. *Proceedings of the Royal Society of London* **102**, 161–179 (1922).

[36] Zöttl, A. & Stark, H. Nonlinear Dynamics of a Microswimmer in Poiseuille Flow. *Physical Review Letters* **108**, 218104 (2012).

[37] Zöttl, A. & Stark, H. Periodic and quasiperiodic motion of an elongated microswimmer in Poiseuille flow. *the European Physical Journal E* **36**, 4 (2013).

[38] Rusconi, R., Guasto, J. S. & Stocker, R. Bacterial transport suppressed by fluid shear. *Nature Physics* **10**, 212–217 (2014).

[39] Chilukuri, S., Collins, C. H. & Underhill, P. T. Impact of external flow on the dynamics of swimming microorganisms near surfaces. *Journal of Physics: Condensed Matter* **26**, 115101 (2014).

[40] Barry, M. T., Rusconi, R., Guasto, J. S. & Stocker, R. Shear-induced orientational dynamics and spatial heterogeneity in suspensions of motile phytoplankton. *Journal of the Royal Society Interface* **12**, 20150791 (2015).

[41] Mathijssen, A. J. T. M., Doostmohammadi, A., Yeomans, J. M. & Shendruk, T. N. Hotspots of boundary accumulation: Dynamics and statistics of micro-swimmers in flowing films. *Journal of the Royal Society Interface* **13**, 20150936 (2016).

[42] Junot, G. *et al.* Swimming bacteria in Poiseuille flow: The quest for active Bretherton-Jeffery trajectories. *Europhysics Letters* **126**, 44003 (2019).

[43] Marcos, Fu, H. C., Powers, T. R. & Stocker, R. Bacterial rheotaxis. *Proceedings of the National Academy of Sciences of the U. S. A.* **109**, 4780–4785 (2012).

[44] Ishikawa, T. *et al.* Separation of motile bacteria using drift velocity in a microchannel. *Lab on a Chip* **14**, 1023–1032 (2014).

[45] Jing, G., Zöttl, A., Clément, É. & Lindner, A. Chirality-induced bacterial rheotaxis in bulk shear flows. *Science Advances* **6**, eabb2012 (2020).

[46] Molaei, M. & Sheng, J. Succeed escape: Flow shear promotes tumbling of Escherichia colinear a solid surface. *Scientific Reports* **6**, 35290 (2016).

[47] Hill, J., Kalkanci, O., McMurry, J. L. & Koser, H. Hydrodynamic Surface Interactions Enable Escherichia Coli to Seek Efficient Routes to Swim Upstream. *Physical Review Letters* **98**, 068101 (2007).

[48] Kaya, T. & Koser, H. Direct upstream motility in Escherichia coli. *Biophysical Journal* **102**, 1514–1523 (2012).

[49] Mathijssen, A. J. T. M., Shendruk, T. N., Yeomans, J. M. & Doostmohammadi, A. Upstream Swimming in Microbiological Flows. *Physical Review Letters* **116**, 028104 (2016).

[50] Figueroa-Morales, N. *et al.* Living on the edge: Transfer and traffic of E. coli in a confined flow. *Soft Matter* **11**, 6284–6293 (2015).

[51] Dey, R., Buness, C. M., Hokmabad, B. V., Jin, C. & Maass, C. C. Oscillatory rheotaxis of artificial swimmers in microchannels. *Nature Communications* **13**, 2952 (2022).

[52] Zheng, H. *et al.* Swimming of buoyant bacteria in quiescent medium and shear flows. *Langmuir* **39**, 4224–4232 (2023).

[53] Zöttl, A. *et al.* Asymmetric bistability of chiral particle orientation in viscous shear flows. *Proceedings of the National Academy of Sciences of the U. S. A.* **120**, e2310939120 (2023).

[54] Mathijssen, A. J. T. M. *et al.* Oscillatory surface rheotaxis of swimming E. coli bacteria. *Nature Communications* **10**, 3434 (2019).

[55] Stoodley, P., Dodds, I., Boyle, J. D. & Lappin-Scott, H. M. Influence of hydrodynamics and nutrients on biofilm structure. *Journal of Applied Microbiology* **85**, 19S–28S (1998).

[56] Conrad, J. C. & Poling-Skutvik, R. Confined Flow: Consequences and Implications for Bacteria and Biofilms. *Annual Review of Chemical and Biomolecular Engineering* **9**, 175–200 (2018).

[57] Hartmann, R. *et al.* Emergence of three-dimensional order and structure in growing biofilms. *Nature Physics* **15**, 251–256 (2019).

[58] Rossy, T., Nadell, C. D. & Persat, A. Cellular advective-diffusion drives the emergence of bacterial surface colonization patterns and heterogeneity. *Nature Communications* **10**, 2471 (2019).

[59] Rusconi, R., Lecuyer, S., Guglielmini, L. & Stone, H. A. Laminar flow around corners triggers the formation of biofilm streamers. *Journal of the Royal Society Interface* **7**, 1293–1299 (2010).

[60] Drescher, K., Shen, Y., Bassler, B. L. & Stone, H. A. Biofilm streamers cause catastrophic disruption of flow with consequences for environmental and medical systems. *Proceedings of the National Academy of Sciences of the U. S. A.* **110**, 4345–4350 (2013).

[61] Miño, G. L. *et al.* E coli Accumulation behind an Obstacle. *Advances in Microbiology* **8**, 451–464 (2018).

[62] Lee, S. H., Secchi, E. & Kang, P. K. Rapid formation of bioaggregates and morphology transition to biofilm streamers induced by pore-throat flows. *Proceedings of the National Academy of Sciences of the U. S. A.* **120**, e2204466120 (2023).

[63] Tsai, Y.-P. Impact of flow velocity on the dynamic behaviour of biofilm bacteria. *Biofouling* **21**, 267–277 (2005).

[64] Wang, S., Zhu, H. Y., Zheng, G. X., Dong, F. & Liu, C. X. Dynamic changes in biofilm structures under dynamic flow conditions. *Applied and Environmental Microbiology* **88**, e01072–22 (2022).

[65] Cremer, J. *et al.* Effect of flow and peristaltic mixing on bacterial growth in a gut-like channel. *Proceedings of the National Academy of Sciences of the U. S. A.* **113**, 11414–11419 (2016).

[66] Wei, G. J. & Yang, J. Q. Microfluidic investigation of the impacts of flow fluctuations on the development of biofilms. *Npj Biofilms and Microbiomes* **9**, 73 (2023).

[67] Cremer, J., Arnoldini, M. & Hwa, T. Effect of water flow and chemical environment on microbiota growth and composition in the human colon. *Proceedings of the National Academy of Sciences of the U. S. A.* **114**, 6438–6443 (2017).

[68] Uppal, G. & Vural, D. C. Shearing in flow environment promotes evolution of social behavior in microbial populations. *eLife* **7**, e34862 (2018).

[69] Labavić, D., Loverdo, C. & Bitbol, A.-F. Hydrodynamic flow and concentration gradients in the gut enhance neutral bacterial diversity. *Proceedings of the National Academy of Sciences of the U. S. A.* **119**, e2108671119 (2022).

[70] Wong, J. P. H., Fischer-Stettler, M., Zeeman, S. C., Battin, T. J. & Persat, A. Fluid flow structures gut microbiota biofilm communities by distributing public goods. *Proceedings of the National Academy of Sciences of the U. S. A.* **120**, e2217577120 (2023).

[71] Wu, Y. *et al.* Cooperative microbial interactions drive spatial segregation in porous environments. *Nature Communications* **14**, 4226 (2023).

[72] Scheidweiler, D. *et al.* Spatial structure, chemotaxis and quorum sensing shape bacterial biomass accumulation in complex porous media. *Nature Communications* **15**, 191 (2024).

[73] Colin, R., Zhang, R. & Wilson, L. G. Fast, high-throughput measurement of collective behaviour in a bacterial population. *Journal of the Royal Society, Interface* **11**, 20140486 (2014).

[74] Darwin, C. Note on hydrodynamics. *Mathematical Proceedings of the Cambridge Philosophical Society* **49**, 342–354 (1953).

[75] Mathijssen, A. J. T. M., Pushkin, D. O. & Yeomans, J. M. Tracer trajectories and displacement due to a micro-swimmer near a surface. *Journal of Fluid Mechanics* **773**, 498–519 (2015).

[76] Jin, C., Chen, Y., Maass, C. C. & Mathijssen, A. J. T. M. Collective Entrainment and Confinement Amplify Transport by Schooling Microswimmers. *Physical Review Letters* **127**, 088006 (2021).

[77] Hernández-Ortiz, J. P., de Pablo, J. J. & Graham, M. D. NlogN method for hydrodynamic interactions of confined polymer systems: Brownian dynamics. *The Journal of Chemical Physics* **125**, 164906 (2006).

[78] Danese, P. N., Pratt, L. A., Dove, S. L. & Kolter, R. The outer membrane protein, antigen 43, mediates cell-to-cell interactions within biofilms. *Molecular Microbiology* **37**, 424–432 (2000).

[79] Kjaergaard, K., Schembri, M. A., Ramos, C., Molin, S. & Klemm, P. Antigen 43 facilitates formation of multispecies biofilms. *Environ Microbiol* **2**, 695–702 (2000).

[80] Besharova, O., Suchanek, V. M., Hartmann, R., Drescher, K. & Sourjik, V. Diversification of gene expression during formation of static submerged biofilms by escherichia coil. *Front. Microbiol.* **7**, 1568 (2016).

[81] Alapan, Y. *et al.* Microrobotics and microorganisms: Biohybrid autonomous cellular robots. *Annual Review of Control, Robotics, and Autonomous Systems, Vol 2* **2**, 205–230 (2019).

[82] Nosrati, R. *et al.* Microfluidics for sperm analysis and selection. *Nature Reviews Urology* **14**, 707–730 (2017).

[83] Grognot, M. & Taute, K. M. More than propellers: how flagella shape bacterial motility behaviors. *Current Opinion in Microbiology* **61**, 73–81 (2021).

[84] Laganenka, L., Colin, R. & Sourjik, V. Chemotaxis towards autoinducer 2 mediates autoaggregation in Escherichia coli. *Nature Communications* **7**, 12984 (2016).

[85] Barnhart, M. M. & Chapman, M. R. Curli Biogenesis and Function. *Annual Review of Microbiology* **60**, 131–147 (2006).

[86] Suchanek, V. M. *et al.* Chemotaxis and cyclic-di-GMP signalling control surface attachment of Escherichia coli. *Molecular Microbiology* **113**, 728–739 (2020).

[87] Mucha, P. J., Tee, S. Y., Weitz, D. A., Shraiman, B. I. & Brenner, M. P. A model for velocity fluctuations in sedimentation. *Journal of Fluid Mechanics* **501**, 71–104 (2004).

[88] Amann, E., Ochs, B. & Abel, K. J. Tightly regulated tac promoter vectors useful for the expression of unfused and fused proteins in escherichia-coli. *Gene* **69**, 301–315 (1988).

Supplementary material

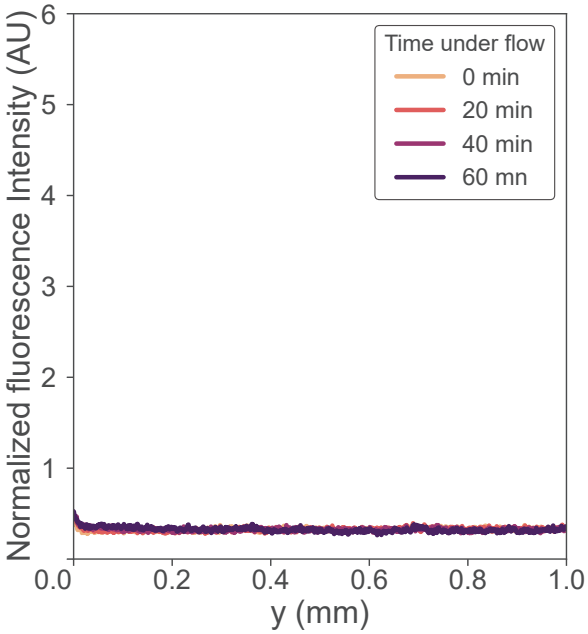

Fig. S1: The distribution of motile cells remains homogeneous in time under shear flow. Distribution of motile cells in the channel over one hour ($\phi_M = 0.17\%$, $\phi_{NM} = 1.7\%$, shear $\dot{\gamma} = 7.5\ s^{-1}$). The small increase in intensity at the left side of the channel (0 mm) is attributed to bleedthrough fluorescence from accumulating non-motile particles.

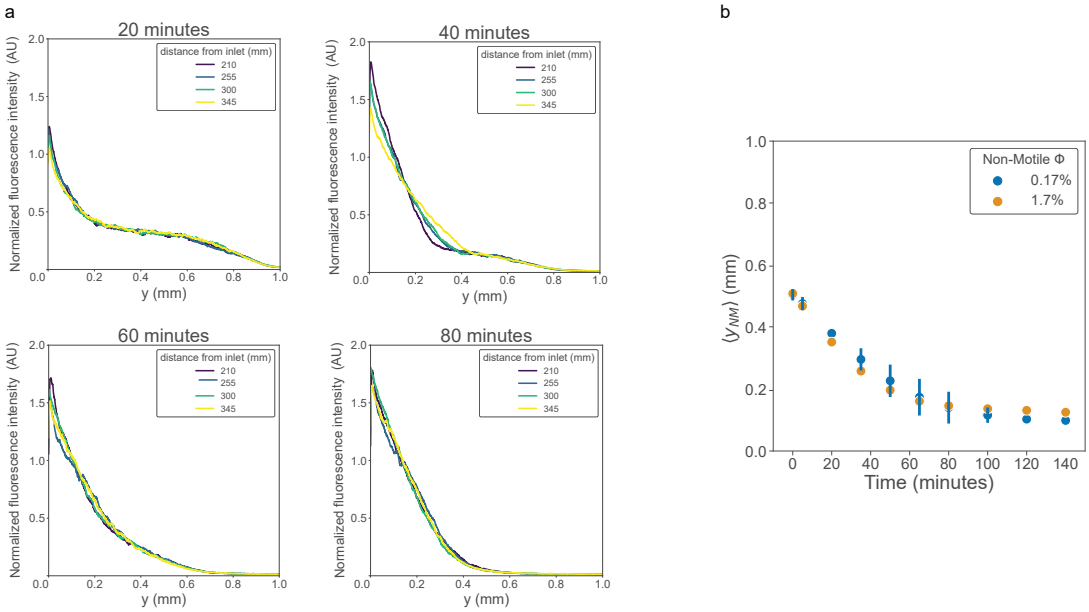

Fig. S2: The accumulation of non-motile cells on the left side is independent of the position in the microfluidic chip and the concentration of non-motile cells. **a** Density profile of non-motile cells at different times for different positions in the microfluidic channel. **b** Position of the center of mass of non-motile cells over time for different concentrations of non-motile cells ($\phi_M = 0.17\%$, shear $\dot{\gamma} = 7.5\ s^{-1}$). Vertical bars represent the standard deviation (SD) over N = 3 biological replicates.

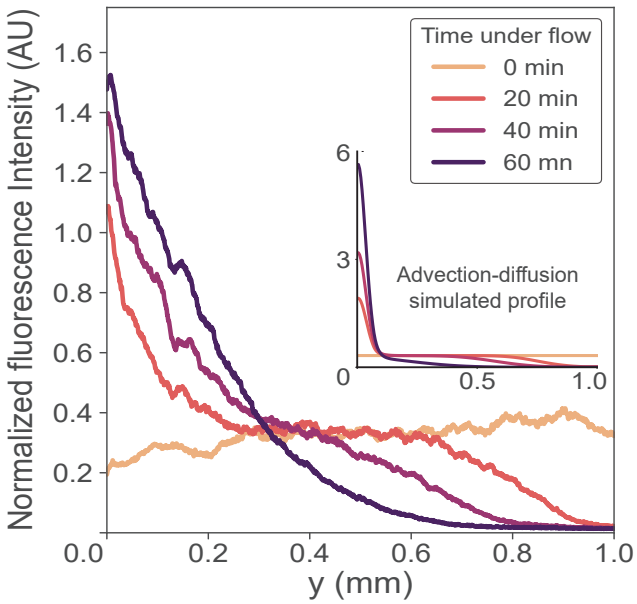

Fig. S3: Density profile of non-motile cell distribution in the channel at 8 μm from the bottom surface obtained from fluorescence images, at high non-motile density ($\phi_M = 0.17\%$, $\phi_{NM} = 1.7\%$, shear $\dot{\gamma} = 7.5\ s^{-1}$). In the inset, simulation results were obtained by solving the one-dimensional advection-diffusion equation. For high concentrations of non-motile particles, the advection-diffusion model fails to capture precisely the accumulation dynamics possibly due to volumetric effects.

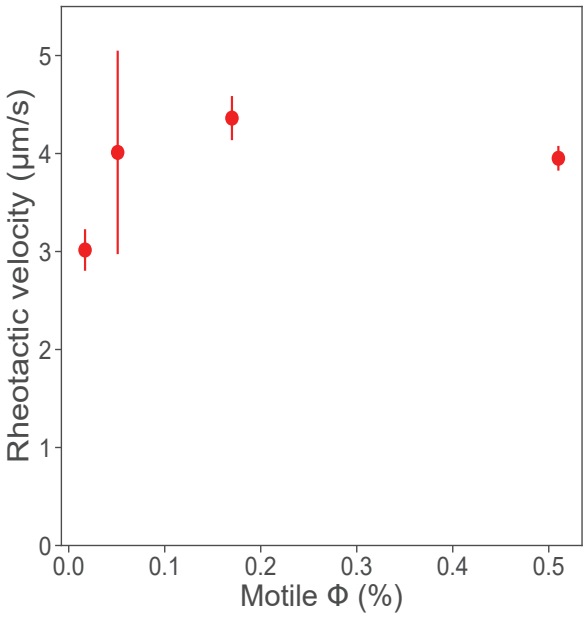

Fig. S4: Measured rheotactic drift of motile cells at different motile volume fractions. For all the experiments, the volume fraction of labeled motile cells is kept constant at $3.4\,10^{-4}$ %, the rest being unlabeled to facilitate tracking, the non-motile volume fraction is $\phi_{NM} = 0.17\%$ (unlabeled to prevent any bleedthrough), and flow shear is set at $\dot{\gamma} = 7.5\ s^{-1}$. Error bars represent the standard deviation (SD) over N = 3 technical replicates.

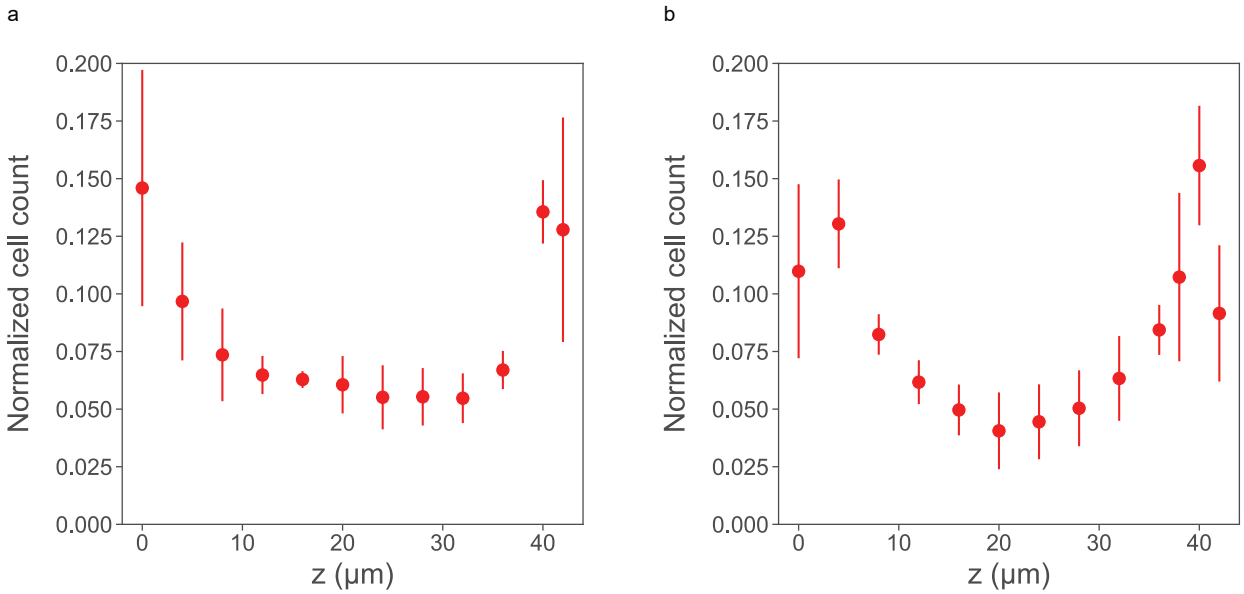

Fig. S5: Motile cells distribute predominantly near the top and bottom surfaces both in the absence (**a**) and presence of flow (**b**). The cells are counted analyzing fluorescence images obtained in the absence of sedimentation with particle tracking. The cell count at each point is normalized to the total cell number of the respective biological replicate. For both experiments, $\phi_M = 0.17\%$, $\phi_{NM} = 1.7\%$ (unlabeled). (**b**) Flow shear at the bottom is set at $\dot{\gamma} = 7.5$). Error bars represent the standard deviation (SD) over N = 3 biological replicates.

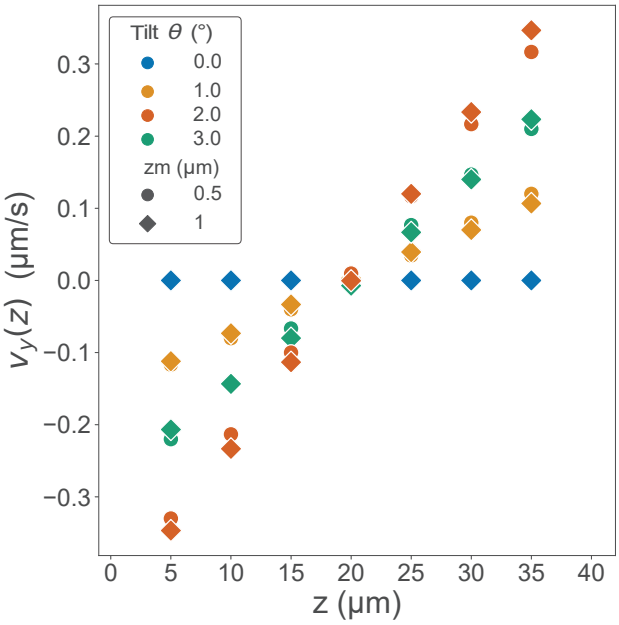

Fig. S6: The distance between the surface and the body of simulated swimmers has a negligible impact on the rheotactic flow in the channel. Simulated component of the flow in the y direction generated in the volume of the channel by a distribution of swimmers (ϕ =0.17 %) and averaged across the x direction, for varying tilts θ toward the surface and for 2 distances of the body of the swimmers from the surface. The orientations of the swimmers are randomly extracted from the distribution measured for a shear of 7.5 s^{-1}

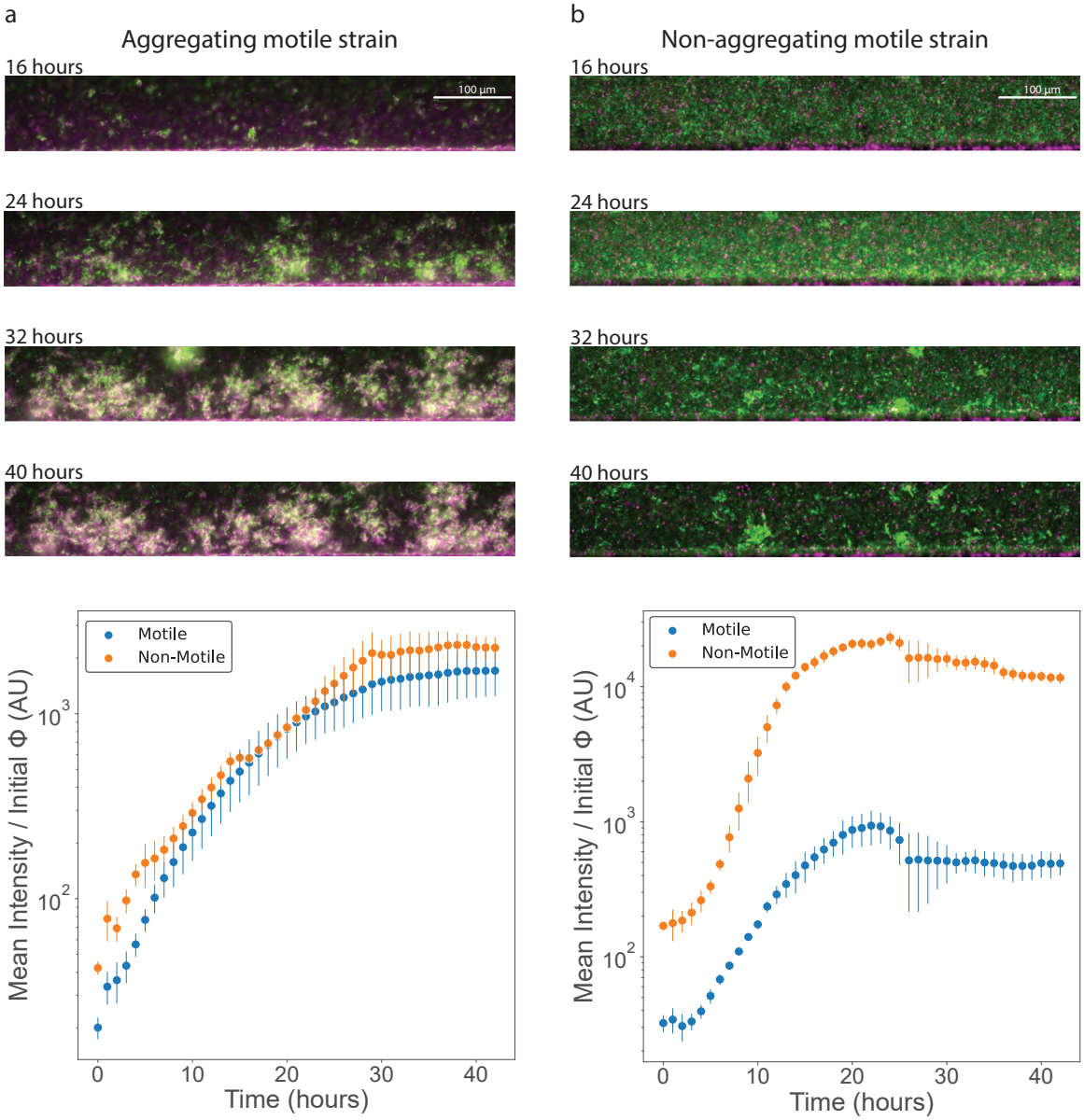

Fig. S7: Aggregating motile bacteria integrate more efficiently into asymmetric biofilms formed by non-motile bacteria than non-aggregating bacteria. **a** View (top) and quantification (bottom) over time for the left side of the channel for a binary mixture with a non-motile fraction (in green) able to form biofilms and a motile fraction (in magenta) able to aggregate. Over time, aggregating motile cells are progressively integrated into the biofilm. **b** View (top) and quantification (bottom) over time of the left side of the channel for a mixture with non-aggregating (Δag43) motile bacteria (magenta). Over time, non-aggregating motile cells form an even mat on the bottom surface of the channel. (**a**,**b**) The mean fluorescence intensity of motile and non-motile cells was measured near the left side of the channel (667 μm x 150 μm) and normalized by the initial volume fraction of the respective strain. The initial volume fractions are $\phi_M = 0.17\%$, $\phi_{NM} = 0.051\%$

Name	Relevant genotype	Source
Strains		
W3110 RH	wild-type	[84]
RC111 (Δ*fliC*)	W3110 RH Δ*fliC* Δ*flu*	[7]
RC86 (Δ*cheY*)	W3110 RH Δ*cheY* Δ*flu*	[7]
RC101 (WT)	W3110 RH Δ*flu* pOB2; AmpR	[7]
RC125 (Δ*cheY*)	W3110 RH Δ*cheY* Δ*flu* pOB2; AmpR	[7]
RC113 (Δ*fliC*)	W3110 RH Δ*fliC* Δ*flu* pOB35; AmpR	[7]
RC114 (Δ*fliC*)	W3110 RH Δ*fliC* Δ*flu* pOB2; AmpR	[7]
SEB21 (Δ*fliC*)	W3110 RH Δ*fliC* pOB35; AmpR	[7]
RC144 (WT)	W3110 RH pOB2; AmpR	[7]
Plasmids		
pTrc99a	Expression vector; pBR ori, pTrc promoter, IPTG inducible; AmpR	[88]
pOB2	*mCherry* in pTrc99A, IPTG inducible; AmpR	[7]
pOb35	*mNeonGreen* in pTrc99A, IPTG inducible; AmpR	[7]

Table S1: Strains used in this study. AmpR: ampicillin resistant